

Creating Binary Cu–Bi Compounds via High-Pressure Synthesis: A Combined Experimental and Theoretical Study

Samantha M. Clarke,^{†,#} Maximilian Amsler,^{‡,#} James P. S. Walsh,[†] Tony Yu,^{||} Yanbin Wang,^{||} Yue Meng,[⊥] Steven D. Jacobsen,[§] Chris Wolverton,^{*,‡,§} and Danna E. Freedman^{*,†,§}

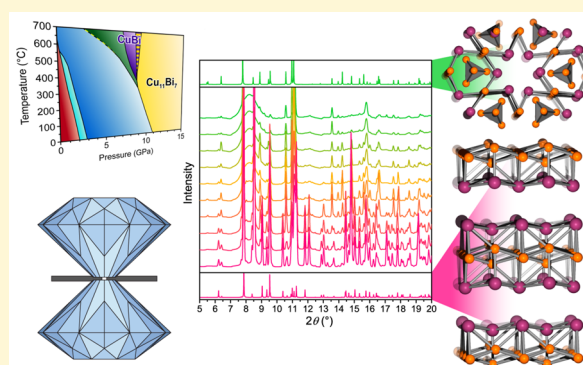
[†]Department of Chemistry, [‡]Department of Materials Science and Engineering, and [§]Department of Earth and Planetary Sciences, Northwestern University, Evanston, Illinois 60208, United States

^{||}GeoSoilEnviroCARS, Center for Advanced Radiation Sources, The University of Chicago, Chicago, Illinois 60637, United States

[⊥]HPCAT, Geophysical Laboratory, Carnegie Institution of Washington, Argonne, Illinois 60439, United States

Supporting Information

ABSTRACT: Exploration beyond the known phase space of thermodynamically stable compounds into the realm of metastable materials is a frontier of materials chemistry. The application of high pressure in experiment and theory provides a powerful vector by which to explore this uncharted phase space, allowing discovery of complex new structures and bonding in the solid state. We harnessed this approach for the Cu–Bi system, where the realization of new phases offers potential for exotic properties such as superconductivity. This potential is due to the presence of bismuth, which, by virtue of its status as one of the heaviest stable elements, forms a critical component in emergent materials such as superconductors and topological insulators. To fully investigate and understand the Cu–Bi system, we welded theoretical predictions with experiment to probe the Cu–Bi system under high pressures. By employing the powerful approach of in situ X-ray diffraction in a laser-heated diamond anvil cell (LHDAC), we thoroughly explored the high-pressure and high-temperature (high-*PT*) phase space to gain insight into the formation of intermetallic compounds at these conditions. We employed density functional theory (DFT) calculations to calculate a pressure versus temperature phase diagram, which correctly predicts that CuBi is stabilized at lower pressures than Cu₁₁Bi₇, and allows us to uncover the thermodynamic contributions responsible for the stability of each phase. Detailed comparisons between the NiAs structure type and the two high-pressure Cu–Bi phases, Cu₁₁Bi₇ and CuBi, reveal the preference for elemental segregation within the Cu–Bi phases, and highlight the unique channels and layers formed by ordered Cu vacancies. The electron localization function from DFT calculations account for the presence of these “voids” as a manifestation of the lone pair orientation on the Bi atoms. Our study demonstrates the power of joint experimental–computational work in exploring the chemistry occurring at high-*PT* conditions. The existence of multiple high-pressure-stabilized phases in the Cu–Bi binary system, which can be readily identified with in situ techniques, offers promise for other systems in which no ambient pressure phases are known to exist.



INTRODUCTION

In the quest for new metastable materials with exotic properties, high-pressure and high-temperature (high-*PT*) synthesis offers tremendous promise. In particular, the emerging technique of in situ monitoring of high-pressure intermetallic syntheses using diamond anvil cells (DACs) enables the rapid synthesis of intermetallic compounds at geophysically relevant pressures. Metastable compounds accessed by this unconventional route exhibit structural complexity, unique bonding, and exotic properties. Indeed, the compounds LaBi¹ and FeBi₂,^{2,3} which were both accessed through high-pressure synthesis, exhibit pressure-induced superconductivity and the first Fe–Bi bond in the solid state, respectively. Rational, hypothesis-driven exploration within high-pressure phase space offers a route toward uncovering

interesting and potentially unprecedented physical phenomena. Significant improvements made recently in computational structure prediction⁴ and in modeling of the enthalpy landscape at high pressure enable guided exploration within the high-pressure realm. Through interfacing in situ high-*PT* synthesis with phase stability calculations, we can expedite the discovery of new materials.

We selected the copper–bismuth binary system for exploration due to the propensity of bismuth to create emergent materials, both in its elemental form and as a component in binary intermetallic compounds. Elemental

Received: April 6, 2017

Revised: June 1, 2017

Published: June 2, 2017

bismuth is remarkable for a variety of reasons, most notably its anomalous electronic properties.^{5–7} Emblematic of bismuth's unusual properties is the recent unexpected discovery of bulk superconductivity in pure elemental bismuth, which defies the conventional Bardeen–Cooper–Schrieffer theory used to describe all other elemental superconductors.⁸ The promise of bismuth binaries is significant, and during the 1960s, several prominent researchers pursued high-*PT* synthesis to isolate novel transition metal–bismuth binary compounds.⁹ During that time, numerous phases were detected, but few were fully characterized due to poor yields and high structural complexity. Indeed, most of these phases were not even identified by stoichiometry. Decades later, returning to this phase space offers the potential to discover new phases, including perhaps phases that previous researchers detected, but were unable to characterize.

Bismuth is unusually well-suited as a reagent for high-pressure syntheses. It is highly unreactive toward intermetallic compound formation with many transition metals under ambient pressures,^{10–13} to the extent it is commonly referred to as an “inert flux”. Once under pressure, bismuth displays a complex energy landscape with a plethora of high-pressure polymorphs,^{14–19} each exhibiting different bonding properties and structural motifs. This ability to form bonds of varying orders and geometries makes high-pressure synthesis an attractive technique for the isolation of binary intermetallic compounds.

Inspired by the prospect of investigating the chemistry of intermetallic formation at high-*PT* conditions, we explored the Cu–Bi binary system. In a recent paper, we performed a joint computational and theoretical study wherein we reported the first structurally characterized intermetallic compound in the Cu–Bi system, Cu₁₁Bi₇. We synthesized Cu₁₁Bi₇ by high-*PT* methods and used computational methods to predict its stability at high pressures. A combination of experiment and theory demonstrated superconductivity below 1.36 K.²⁰ Recently, a second superconducting compound in this binary system, CuBi, was isolated, again using high-*PT* methods.²¹ Herein, we report a combined high-pressure synthetic and theoretical exploration of the rich Cu–Bi binary system. By combining in situ X-ray diffraction experiments at high-*PT* conditions with density functional theory (DFT)-based structure prediction and phase stability calculations, we probe the vast phase space of the Cu–Bi system, and begin to gain insight into formation dynamics of these new intermetallic compounds. The electron localization function from DFT calculations of CuBi and Cu₁₁Bi₇ highlight the stereochemical activity of the lone pair on the Bi atoms and emphasize the formation of layers and channels in these compounds. The rich chemistry in the high-pressure Cu–Bi system highlights the potential for the uncharted high-pressure phase space in other systems.

RESULTS AND DISCUSSION

Exploration of the Copper–Bismuth System.

We targeted the synthesis of novel copper–bismuth binaries between 0–10 GPa due to the wealth of elemental high-pressure bismuth polymorphs that exist over this pressure range. We hypothesized that boundaries between the high-pressure elemental phases of bismuth would be fertile sites for the formation of new binary compounds. To gain insight into this system, we performed small-scale high-pressure reactions of elemental copper and bismuth in a laser-heated diamond anvil

cell (LHDAC). Using synchrotron-based powder X-ray diffraction (PXRD) experiments performed in situ at variable temperatures under multiple pressures, we can begin to map out the experimental high-pressure phase diagram for the Cu–Bi system. In addition, such experiments can provide unique insight into formation dynamics and can facilitate the optimization of materials synthesis. In these experiments, small amounts of elemental Cu and Bi are placed in the LHDAC and compressed to the desired pressure (Figure S2). MgO is used as a thermal insulator between the sample and the diamond anvils and also assists in transmitting the pressure evenly throughout the cell. Further, the well-defined equation of state of MgO allows for the precise determination of pressure for each reaction.²² After achieving the desired pressure, we heated the elemental mixture using an infrared laser focused to a fwhm of $\sim 40 \mu\text{m}$, and we continuously monitored the reaction using in situ PXRD ($\lambda = 0.406626 \text{ \AA}$, X-ray diameter of $\sim 5\text{--}10 \mu\text{m}$) at beamline 16-ID-B, HPCAT, Advanced Photon Source (APS).²³ Figure 1 highlights the results of the in situ PXRD experiments performed at multiple pressures.

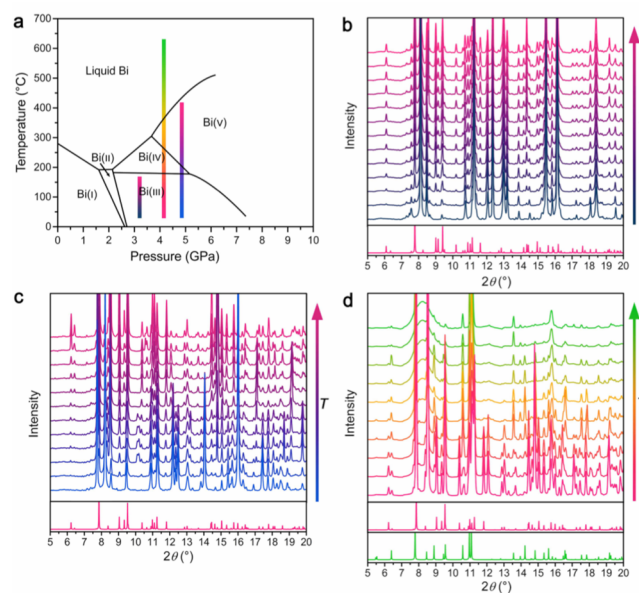


Figure 1. (a) Temperature versus pressure phase diagram for elemental Bi depicting the five different high-pressure polymorphs of bismuth (taken from ref 19). Vertical colored bars represent the approximate temperatures and pressures investigated using in situ X-ray diffraction in this study. Panels b–d show background-subtracted in situ PXRD patterns collected while heating mixtures of elemental Cu and Bi at various pressures and temperatures ($\lambda = 0.406626 \text{ \AA}$). The simulated powder pattern of the new Cu–Bi phase formed is plotted below the experimental data (CuBi in pink and Cu₁₁Bi₇ in green). (b) Reaction at 3.19(1) GPa leads to the creation of CuBi as a minor phase. (c) Reaction at 4.88(1) GPa leads to peaks of CuBi increasing in intensity with increasing temperature. Peaks at $\sim 10.1^\circ$ indicate the transformation of Bi(III) into Bi(IV). The peak at 8.2° decreasing in intensity and the peak at 8.5° increasing in intensity indicate the transformation of Bi(IV) to Bi(V). (d) Heating of a prereacted area at 4.16(1) GPa shows the formation of Cu₁₁Bi₇ from CuBi and elemental Bi and Cu. Formation of this phase occurs at the melting point of elemental Bi, which is indicated by the broad intensity from $7\text{--}10^\circ$.

The *PT* stability of the five elemental polymorphs of Bi is shown in the temperature versus pressure phase diagram for elemental Bi (Figure 1a).¹⁹ There are no known high-pressure Cu polymorphs, and Cu melts at or above 1085 °C at all pressures. Therefore, elemental fcc Cu is stable over the entire region shown in Figure 1a.²⁴ The vertical colored bars in this figure represent the approximate pressures and temperatures investigated using the in situ XRD technique. The in situ diffraction patterns (Figure 1b–d) collected at regular intervals during heating reveal the formation of either CuBi (pink) or Cu₁₁Bi₇ (green) at different *PT* conditions. Figure 1b shows the reaction of the elements at ~3.19(1) GPa. In this reaction, we gradually increased the laser power, thereby heating the elemental reactants, Cu and Bi(III), from room temperature to ~150 °C. Because temperatures in this range are difficult to monitor precisely, we inferred the upper limit of temperature from the lack of Bi(IV) peaks, which are expected to grow in above 150 °C. Characteristic peaks belonging to CuBi begin to appear (most noticeably at 6.1°, 7.8°, and 10.2°), at which point we held the laser at constant power for 10 min. The peaks grow in intensity for approximately 4 min, at which point no further changes are observed. The reaction was thermally quenched by turning off the laser. Evaluation of the powder diffraction pattern acquired after cooling confirmed the presence of CuBi along with elemental Bi(III) and Cu. This experiment illustrates that the synthetic conditions for the formation of CuBi are at relatively low pressures and temperatures (3.2 GPa, <160 °C), far below the melting point of elemental Bi at that pressure. Therefore, the formation of CuBi progresses through a solid-state diffusion process that does not rely on the presence of elemental liquid Bi. Additionally, we determined that CuBi and some residual, unreacted elemental Cu and Bi coexist at these *PT* conditions.

To investigate the formation of Cu–Bi compounds at slightly higher pressures, we reacted elemental copper and bismuth in a LHDAC at ~4.88(1) GPa (Figure 1c). Again, elemental reactants were heated by gradually increasing the laser power. At low power, it is apparent that CuBi is already forming based on the appearance of peaks at ~9° and 11.8°. At slightly higher power, peaks appear at ~10.1°, indicating the transformation of Bi(III) into Bi(IV). In the Bi *PT* phase diagram, this structural phase change occurs above 177 °C, allowing us to establish that the formation of CuBi begins below this temperature. As the laser power is further increased, the transformation of Bi(IV) to Bi(V) is indicated by the decrease in intensity of the peaks at ~10.1° and 8.2°, and the appearance of a peak at 8.5°. This phase change occurs above 200 °C at this pressure, demonstrating how elemental structural phase changes of Bi can be used to estimate temperature during the in situ experiment. Throughout the entire reaction, the intensities of the CuBi peaks are increasing, indicating that higher temperatures stabilize the formation of CuBi relative to the reactants. Upon cooling, the CuBi phase remains and the Bi(V) reconverts to Bi(III).

To explore the reaction of Cu with liquid Bi at high temperatures, a third reaction was performed at a starting pressure of 4.16(1) GPa. In this reaction, a prereacted area containing CuBi, Cu, and Bi(III) was heated from ambient temperature to above the melting point of elemental Bi, as indicated by the broad intensity from 7–10° arising from liquid Bi (Figure 1d). This elemental phase change indicates that the reaction temperature was greater than 350 °C. For this reaction, the temperature was also measured by fitting the visible portion

of the blackbody emission to the Planck radiation function and was found to reach ~800 °C. As the temperature is increased, the amount of liquid Bi increases, and CuBi gradually transforms into Cu₁₁Bi₇. This may suggest that at 4.2 GPa and high temperatures, Cu₁₁Bi₇ is the thermodynamically stable phase. As the temperature is further increased, the intensity of the peaks corresponding to Cu₁₁Bi₇ decrease and the intensity of the broad peak corresponding to liquid Bi increases. Upon cooling, a very small amount of Cu₁₁Bi₇ remains, with the majority of the product being elemental Bi(III). This experiment suggests that Cu₁₁Bi₇ is synthesized through a melting process, rather than through a solid-state diffusion process, at these pressures. This hypothesis was corroborated by the successful synthesis of Cu₁₁Bi₇ in a multi-anvil press (MAP) at the melting point of Bi(V) (~530 °C) under a pressure of ~6 GPa.

From these in situ diffraction experiments, we can begin to construct an experimental phase diagram. From the lower temperature experiments, we know that between 3.2 and 4.8 GPa and below the melting point of elemental Bi, CuBi is the thermodynamically stable phase. By probing the temperatures above the melting point of elemental Bi at 4.2 GPa, we learned that CuBi transforms into the high-temperature stabilized phase, Cu₁₁Bi₇, with the excess bismuth forming bismuth metal. Clearly, the use of in situ diffraction provides valuable insight into formation dynamics of these new intermetallic compounds, and has the immediate potential to increase the efficiency of materials discovery and optimization.

Scale-Up and Isolation of the Binary CuBi. To further probe the structure and properties of these materials, we worked to scale up these reactions. The binary Cu–Bi compounds were obtained in >85% yield by reaction of the elements at high pressures and temperatures using a MAP housed at the Advanced Photon Source. Specifically, CuBi was formed from reaction of the elements at ~4 GPa and ~250 °C for 5 min, and Cu₁₁Bi₇ is formed at ~6 GPa and ~530 °C for 1 h, as has been previously reported.²⁰ The samples were cooled to ambient temperature by switching off the current to the resistive heater, and the samples were slowly decompressed. Our MAP conditions for the synthesis of CuBi are similar to that of a recently reported MAP synthesis of this compound.²¹

The complex high-pressure structures of these compounds are quenchable (i.e., they remain intact at ambient pressures), allowing for their full structural and electronic characterization under ambient conditions. Both compounds are metastable at ambient pressure and temperature, with decomposition temperatures of $T_d = 158$ and 130 °C for CuBi and Cu₁₁Bi₇, respectively, determined via differential scanning calorimetry (Figure S5). The higher decomposition temperature of CuBi indicates a lower metastability (with lower formation energy), which is expected given that it is the lower-pressure stabilized intermetallic.

Structure Descriptions. Because of the layered structure of CuBi, crystals of sufficient size for single-crystal X-ray diffraction could not be isolated from the reaction product synthesized in the MAP. Therefore, the structure was solved by Rietveld refinement of the synchrotron PXRD pattern. The pattern was indexed to the orthorhombic space group *Pmma* with unit cell parameters $a = 5.18899(2)$ Å, $b = 4.23081(2)$ Å, and $c = 7.86634(3)$ Å. A search of the Inorganic Crystal Structure Database (ICSD)²⁵ for known structures with similar symmetry and lattice parameters yielded orthorhombic Mn–(Bi_{0.85}Sb_{0.15}) as a close match.^{26,27} We used the atomic

positions from this structure as a starting point for the refinement of CuBi. The composition determined from energy-dispersive X-ray spectroscopy (EDS) is in excellent agreement with the composition determined from the crystal structure. Notably, concurrent with the experimental structure solutions, we independently performed calculations using the Minima Hopping method that correctly predicted the structure of the CuBi compound. These results are described below.

The complex, commensurately modulated structure of $\text{Cu}_{11}\text{Bi}_7$ was solved using single-crystal X-ray diffraction. Details of the structure solution are explained in an earlier report.²⁰ Briefly, the compound crystallizes in a hexagonal sublattice with additional satellite reflections around the main ones. A (3+1)-dimensional crystallographic approach was used to solve the commensurate supercell in the superspace group $Pm(\alpha 1/2\gamma)s$ with final unit cell parameters $a = 8.5907(4)$ Å, $b = 5.2542(3)$ Å, $c = 8.5931(5)$ Å, $\beta = 120.013(2)^\circ$, and a commensurate modulation vector $q = 1/3a^* + 1/2b^* + 1/3c^*$.

Both structures can be understood by their similarity to the canonical NiAs ($B8_1$) structure type. Figure 2 depicts the

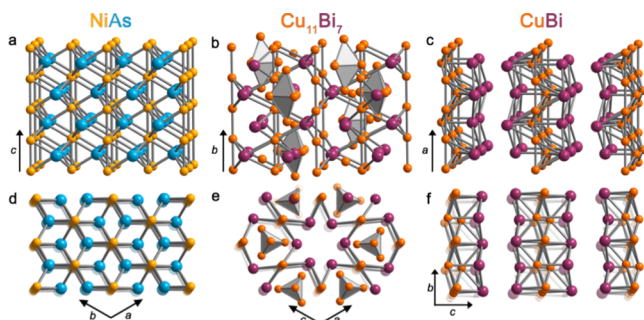


Figure 2. Comparison of the crystal structures of $\text{Cu}_{11}\text{Bi}_7$ (b, e) and CuBi (c, f) with the NiAs structure type (a, d). Yellow, blue, orange, and violet spheres represent Ni, As, Cu, and Bi, respectively. Striking differences from the NiAs structure-type include the trigonal bipyramids formed by the Cu atoms in $\text{Cu}_{11}\text{Bi}_7$ (b) and the trigonal prismatic, square face monocapped interstitial Cu atoms in CuBi (c). View along the transition-metal chain direction shows the Cu vacancies in $\text{Cu}_{11}\text{Bi}_7$ (e) and CuBi (f).

relationship of the novel Cu–Bi structures to that of NiAs. The NiAs structure type is composed of hexagonal close packed (hcp) As (or pnictogen Pn) atoms where the octahedral interstices are occupied by Ni (or transition metal T) atoms (Figure 2a and d).²⁸ The Ni–Ni (or T – T) bonding interaction along the c -axis forms linear Ni chains with short separations ($d = 2.519$ Å). The key differences between this structure type and the new Cu–Bi binary compounds arise from ordered vacancies and interstitial occupancy of the Cu atoms.

The $\text{Cu}_{11}\text{Bi}_7$ binary differs from the NiAs structure type in that an ordered vacancy of the Cu chains generates empty one-dimensional channels formed exclusively of Bi trigonal antiprisms that are face-sharing along the b -axis (Figures 2e and 3b). The opening of these clearly visible channels is estimated to be the distance between a Bi atom and the line formed by the other two Bi atoms belonging to the same plane, which is $d_{\text{ave}} \approx 3.34$ Å. The shortest Bi–Bi bonding interaction is along the b -axis between Bi atoms belonging to different planes ($d_{\text{ave}} \approx 3.44$ Å), and is much longer than what would be expected from doubling the ($2r_{\text{Bi}} = 2.96$ Å),²⁹ suggesting weak Bi–Bi interactions in this compound. Another unique feature of this compound is the presence of Cu_5 trigonal bipyramids,

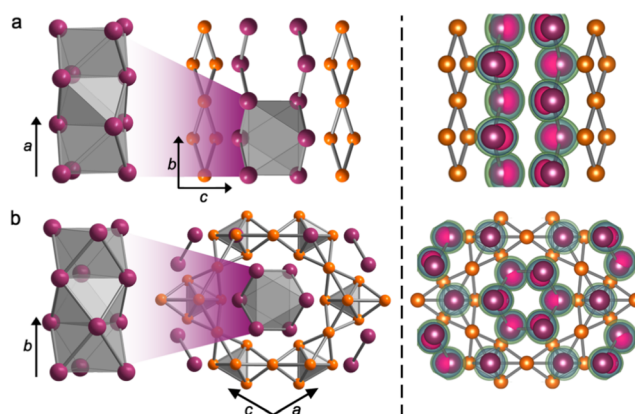


Figure 3. Left panel highlights the pillars formed by the Bi atoms and the crystal structures of CuBi (a) and $\text{Cu}_{11}\text{Bi}_7$ (b), with orange and purple spheres representing Cu and Bi, respectively. Only Cu–Cu and Bi–Bi bonds are drawn to highlight the elemental segregation within the structure. The right panel shows isosurfaces of the electron localization function (ELF), highlighting the voids formed by the bismuth atoms in each structure. ELF isosurface values of 0.7, 0.8, and 0.9 are shown in green, blue, and pink, respectively. The highly localized ELF isosurfaces indicate lone pairs on the Bi atoms that point toward the center of the voids.

which alternate with Bi atoms along the b -axis (Figure 1b). Within the Cu_5 cluster, the Cu–Cu bond distances vary from 2.518–2.580 Å between equatorial Cu atoms to 2.609–2.687 Å between an equatorial and an apical Cu atom. The weaker bonding interaction is likely due to the higher coordination number of the apical Cu atoms (CN = 9) as compared to the equatorial ones (CN = 8).³⁰ The Cu_5 bipyramid structure can be envisioned as capped over all faces by the Cu atoms from the Cu chains, forming a larger Cu_{11} cluster that is apical-vertex-sharing with a dicapped trigonal prismatic coordinated Bi atom along the b -axis (Figure 3b). This larger structure is edge sharing in the ac -plane to form a Cu framework (Figure 3b). There are two shortest Cu–Bi bonds: the first is between the apical Cu_5 atoms and Bi atoms composing the channel ($d_{\text{ave}} \approx 2.77$ Å), and the second is between the trigonal prismatic coordinated Bi atom and the coordinating Cu atoms ($d_{\text{ave}} \approx 2.79$ Å). The rest of the Cu–Bi interactions are greater than the sum of the covalent radii ($r_{\text{Cu}} + r_{\text{Bi}} = 2.81$ Å).²⁹ The well-separated Cu framework and Bi channels represent elemental segregation within the intermetallic compound, which reflects the preference for full segregation of the elements at standard conditions (Figure 2b).

Similar to $\text{Cu}_{11}\text{Bi}_7$, CuBi departs from the NiAs structure type and instead crystallizes in the Co_2InTb structure type.³¹ This structure can be generated from the NiAs structure type by an ordered vacancy of Cu chains, which gives rise to a unique layered structure (Figures 1c,f and S3). An additional Cu2 site within the lattice displaces the Bi atoms to form an overall puckered two-dimensional triangular net of Cu atoms. Within this net, there are two short Cu–Cu bonds between the Cu1 and Cu2 (2.5632(2) Å), a slightly longer bond between two Cu1 atoms (2.5945(0) Å), and one long bond between Cu2 atoms (2.8949(6) Å). The Bi atoms are severely distorted from the hexagonal close packing arrangement found in the NiAs structure type and form a puckered two-dimensional rhombus network. Bond distances between the Bi atoms are 3.3801 Å, which again are significantly longer than doubling the covalent radii of Bi ($2r_{\text{Bi}} = 2.96$ Å).²⁹ The two-dimensional Bi

network is attached to both sides of the Cu net, creating a bonding interaction between the Cu and Bi atoms. Cu1 and Cu2 each have a bonding interaction with Bi1 at a distance of 2.8200(5) and 2.8227(2) Å, respectively, which agrees well with the sum of the covalent radii ($r_{\text{Cu}} + r_{\text{Bi}} = 2.81$ Å).²⁹ The bismuth–copper bonds differ more significantly; there are two Bi2–Cu1 bonds: one is unusually short (2.6816(8) Å), while the second bond is notably long (2.9469(4) Å). The very short bond indicates strong Cu–Bi interactions between these two atoms. Similar to the structure of $\text{Cu}_{11}\text{Bi}_7$, the presence of two-dimensional elemental sheets stacking in a repeating sequence of Bi–Cu–Bi along the *c*-axis reflects the preference for segregation of the elements at standard conditions (Figure 3a).

Of the known binary first row transition-metal–bismuth compounds, both MnBi and NiBi crystallize in the NiAs structure type. The low-temperature phase of MnBi has the ideal NiAs crystal structure; however, a high-temperature phase stable above 340 °C exhibits a disordered NiAs structure type whose exact structure is still debated, but likely contains Mn atoms in interstitial positions.³² Similarly, NiBi has recently been found to have Ni atoms in interstitial positions and partial Ni vacancies in the transition metal chains.^{33,34} From this trend, the interstitial Cu atoms are not unprecedented; however, ordered Cu vacancies that create channels and layers in the novel Cu–Bi intermetallics are certainly unusual. Future work will focus on revealing a correlation between the electronic structure and the absence or presence of electron-lined voids in these materials, and will potentially lead to the targeted design of such layered intermetallic compounds.

Electron Localization Function Calculations. The distinguishing feature of the Cu–Bi binary intermetallic compounds is that of channels and layers formed by bismuth atoms (Figure 3). We attribute these features to nonbonding electrons, or stereochemically active lone pairs, on the Bi atom. The stereochemical activity of lone pairs is frequently observed in compounds containing cationic Bi^{3+} .³⁵ However, the stereochemical activity of Bi atoms in intermetallic compounds is less common. One example of this behavior occurs in RhBi_4 , which features highly localized lone pairs that are located on the Bi atoms and directed into the space between Rh–Bi polyhedral nets.³⁶ These were postulated to correlate with the superconductivity of the material. Another example is the compound IrBi_4 where lone pairs on the Bi atoms are pointing into the voids of the complex network of Bi–Ir polyhedra.³⁷ Beyond these examples, very few studies of the lone pairs in binary intermetallic Bi compounds have been reported, potentially due to the paucity of such materials. Therefore, CuBi and $\text{Cu}_{11}\text{Bi}_7$ add to the distinctive category of bismuth-based intermetallic compounds with stereochemically active lone pairs.

To gain further insight into the unique structural features formed by the Bi atoms, we computed the electron localization function (ELF) of $\text{Cu}_{11}\text{Bi}_7$ and CuBi. High ELF values correspond to regions of high electron localization, such as covalent bonds or lone pairs. The calculated ELF values are limited to the range of 0–1. In the right panel of Figure 3, ELF isosurface values of 0.7, 0.8, and 0.9 are shown in green, blue, and pink, respectively.

A section of the ELF calculation is shown in the *bc*-plane passing through the Bi atoms in CuBi, clearly showing the layered nature of this compound (Figure 3a). The lone pairs of the Bi atoms can be clearly observed between the individual layers, indicated by the pink isosurface at a value of ELF = 0.9.

Similarly, a section of the ELF is shown in the *ab*-plane of $\text{Cu}_{11}\text{Bi}_7$, illustrating the presence of channels in the structure and the preference of the highly localized electrons to point toward the void (Figure 2b). The calculation of such highly localized electrons pointing toward the voids further supports our assignment of stereochemically active lone pairs. To better compare these results to the known binary intermetallic Bi compounds, we computed the ELF of RhBi_4 and IrBi_4 . Figure S7 shows the crystal structures of CuBi, RhBi_4 , and IrBi_4 with the ELF isosurface at a value of 0.93. The Bi atoms in each compound have strongly anisotropic chemical environments, highlighted by nearest-neighbor bonds existing in the direction opposite to the void space. The highly localized electrons point toward these voids within the structures, in the opposite direction of their nearest neighbor bonds. This further supports that the formation of layers and channels in the Cu–Bi compounds is driven by a similar mechanism.

The presence of electron-lined voids in both compounds could facilitate the intercalation of electrophilic species, and could prove to be specifically useful in battery or ionic conductivity applications. The distance from the center to the vertices of the Bi trigonal antiprisms that compose the channels in $\text{Cu}_{11}\text{Bi}_7$ ranges from 2.57 to 2.60 Å. In CuBi, the layer is composed of severely distorted Bi trigonal antiprisms where the distance from the center of the antiprism to Bi2 is 2.29 Å and to Bi1 is 2.86 Å. While the space in both compounds seems rather narrow, there is enough room for the intercalation H^+ and Li^+ , with estimated bismuth contact distances of 1.76 and 2.05 Å, respectively. Surprisingly, there could even be enough room for the intercalation of the alkali-metal cation Na^+ in $\text{Cu}_{11}\text{Bi}_7$, with an expected contact distance of 2.41 Å. These results highlight the potential future chemical utility of these high-pressure solids with electron-lined voids.

Calculated Cu–Bi High-Pressure Phase Diagram. Theoretical methods are useful in predicting novel materials at extreme pressures. The power and accuracy of structure prediction in conjunction with density functional theory calculations have been demonstrated for various materials. For example, the discovery of unexpected stoichiometry in the Na–Cl system³⁸ and the first helium compound³⁹ were both initially predicted from first-principles calculations. To this end, we performed *ab initio* calculations to independently investigate the theoretical stability of the new phases as a function of pressure and temperature.

We carried out structure prediction calculations based on the Minima Hopping method (MHM) at variable compositions to sample the enthalpy landscape at pressures of 0 and 10 GPa. At 0 GPa, we find that the *Pmma* structure of CuBi is the lowest enthalpy structure at the given composition when cells containing 16 or less atoms are explored, with a positive formation enthalpy of 48 meV/atom, indicating that CuBi is indeed metastable at ambient conditions with respect to decomposition into Cu+Bi. The computed lattice parameters at 0 GPa of $a = 5.2036$ Å, $b = 4.26321$ Å, and $c = 8.13071$ Å are in excellent agreement with the experimental results. To our surprise, and in contrast to the $\text{Cu}_{11}\text{Bi}_7$ phase, which only becomes enthalpically stable at pressures above approximately 12 GPa, CuBi has a positive formation enthalpy over all pressures. In fact, the pressure at which CuBi exhibits the smallest formation enthalpy (5.5 meV/atom) is about 14 GPa, a value that is significantly higher than the pressures used to experimentally synthesize CuBi of 3–5 GPa.

Elevated temperatures can promote the formation of compounds and phase transitions in two manners. On one hand, high temperature is required to overcome kinetic barriers that need to be surmounted for a phase transformation. On the other hand, it changes the thermodynamic conditions and can lead to a shift in the stability regimes of different phases. Because the samples of CuBi and $\text{Cu}_{11}\text{Bi}_7$ had been both synthesized at elevated temperatures (above 50 °C, 323 K), we computed the vibrational entropy within the harmonic approximation to assess the Gibbs free energies of formation.

To compute a complete PT phase diagram of the Cu–Bi binary system, we evaluated the stability of the CuBi $Pmma$ phase and the recently discovered high-pressure $\text{Cu}_{11}\text{Bi}_7$ phase with respect to the elements from DFT calculations of free energies as a function of both temperature and pressure. To do this, we must first understand the calculated stability of the elemental high-pressure phases. In contrast to Cu, which remains in the face centered cubic (fcc) structure, elemental bismuth undergoes a series of phase transitions upon compression, which are summarized in Figure 1a. DFT is able to qualitatively reproduce the experimental PT phase diagram for elemental Bi. However, the pressures and temperatures of the transition from Bi(III) to Bi(IV) and from Bi(IV) to Bi(V) are severely overestimated, a behavior of DFT that has been reported before.^{20,40} Note that liquid phases were neglected in our calculations, and that imaginary phonons emerge at conditions where Bi is experimentally reported to melt (denoted by the dashed line in Figure 4). Nevertheless, we

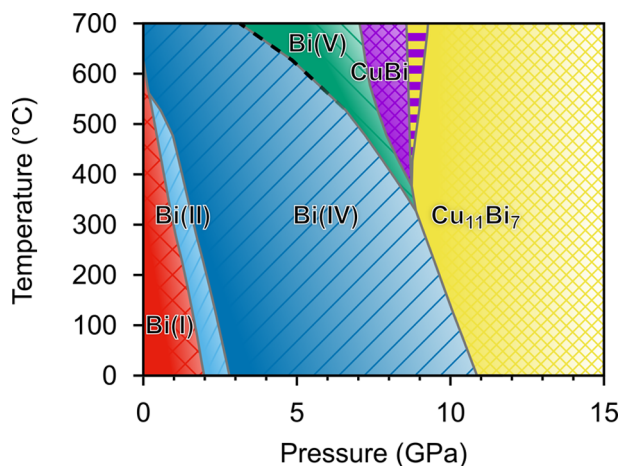


Figure 4. Temperature–pressure phase diagram of the Cu–Bi system derived from the DFT Gibbs free formation energies. The different shaded areas indicate the decomposition into elemental Cu (fcc) and various Bi phases (from left to right, red is Bi(I), teal is Bi(II), blue is Bi(IV), and green is Bi(V)). The violet and yellow areas indicate the PT region where CuBi and $\text{Cu}_{11}\text{Bi}_7$ are thermodynamically stable, respectively. In the striped area, both CuBi and $\text{Cu}_{11}\text{Bi}_7$ are thermodynamically stable. The dashed line indicates the region where Bi(V) becomes dynamically unstable.

can qualitatively construct the phase diagram to assess the PT -stability of CuBi and $\text{Cu}_{11}\text{Bi}_7$ by including the calculated ranges of negative formation free energies of these phases (Figure S8). The phase boundaries of both binaries with respect to elemental decomposition differ significantly from each other. For $\text{Cu}_{11}\text{Bi}_7$, the phase boundary at 0 K is 11.7 GPa and has a negative slope, extending to 7.9 GPa at 1000 K. This suggests that pressure alone would suffice to render $\text{Cu}_{11}\text{Bi}_7$

thermodynamically stable, and elevated temperatures merely decrease the transition pressure (Figure S8b). On the other hand, elevated temperatures are required to reach conditions where CuBi exhibits negative formation free energy (Figure S8a), a necessary condition for thermodynamic stability. In other words, the formation free energy is positive at all pressures at 0 K, and the only way to stabilize CuBi is by increasing the pressure and simultaneously using elevated temperatures.

Besides a negative formation energy, a compound is only thermodynamically stable if its formation free energy lies on the so-called convex hull of stability, that is, if it is lower than those of any combination of competing phases at a given pressure, temperature, and composition. Using this criterion, we can combine the calculated formation free energies of CuBi and $\text{Cu}_{11}\text{Bi}_7$ with the elemental Cu and Bi phases to generate the phase diagram in Figure 4. This combined phase diagram correctly identifies that CuBi is stable at lower pressures as compared to $\text{Cu}_{11}\text{Bi}_7$. Interestingly, the diagram also contains a narrow pressure–temperature region wherein both compounds simultaneously lie on the convex hull of stability and can coexist. However, the significant overestimation of the transition pressures and temperatures of the elemental high-pressure bismuth phases carries on to the Cu–Bi compounds. The main source of this error lies in the very small energy differences between the competing phases, which we use to construct the phase diagram. Different approximations to the exchange correlation functional, for example, can easily shift the phase boundaries. We estimate that the error bars could be as high as ± 5 GPa in pressure and ± 300 K in temperature.

To further understand how pressure influences the stability of CuBi and $\text{Cu}_{11}\text{Bi}_7$, we examined the various contributions to the formation enthalpy (ΔH) at 0 K as a function of pressure (Figure 5). The vertical sections denote the pressure regions where one of the five elemental bismuth phases is enthalpically stable. As mentioned above, there is no pressure region where the formation enthalpy of CuBi is negative, as shown in the top panel of Figure 5 (solid red line), although the magnitude decreases rapidly as the pressure increases. The enthalpy difference, $\Delta H = \Delta E + P\Delta V$, can be decomposed into the internal energy difference, ΔE , and the pressure term, $P\Delta V$, which are shown as dashed blue and dotted orange lines, respectively. In contrast to ΔH , both ΔE and $P\Delta V$ are discontinuous at the boundaries of the various elemental Bi phases. Similar to the enthalpy, the energy term is positive over the whole pressure range. Because ΔE is positive for both compounds, the main driving force for their stabilization must come from one of the other terms in the thermodynamic free formation energy, $\Delta G = \Delta E + P\Delta V - T\Delta S$. Indeed, for CuBi, the pressure term, $P\Delta V$, is negative, and within each section of a Bi allotrope it decreases monotonically. The only exception is with respect to Bi(V), where $P\Delta V$ is slightly positive. At ambient pressure, the voids between the layers in CuBi lead to a high atomic volume, which is larger than the combined volumes of elemental Cu with Bi (III), Bi (IV), or Bi (V). However, due to the high compressibility of CuBi^{41} and the rapid decreases in its volume between 0 and 8 GPa, it asymptotically approaches a value close to Cu + Bi(V). Note that Bi (V) is the most dense among all Bi allotropes. The high compressibility accounts for the $P\Delta V$ term remaining negative up to the Bi(V) phase boundary. Additionally, we show the entropic contribution to the Gibbs free energy $-T\Delta S$ at 700 K as a short-dashed green line. This term is also negative and

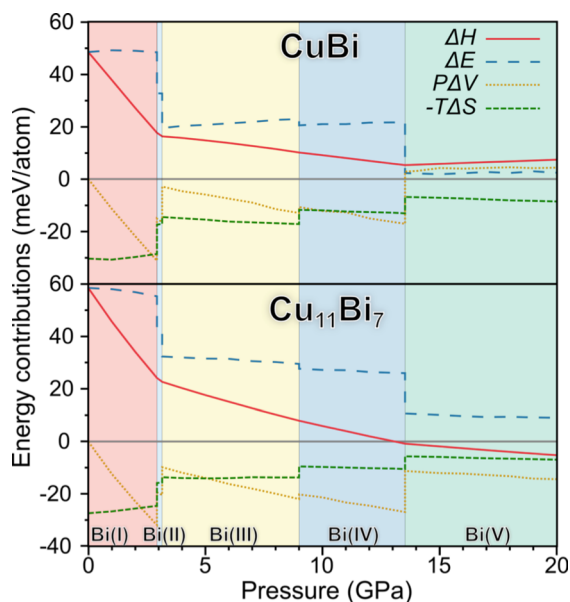


Figure 5. Various energy contributions to the DFT enthalpy difference, $\Delta H = \Delta E + P\Delta V$, for CuBi (top panel) and $\text{Cu}_{11}\text{Bi}_7$ (bottom panel) at 0 K as a function of pressure with respect to elemental decomposition into Cu and the various allotropes of bismuth. The vertical lines separate the regions where different Bi allotropes are favored. Each region is colored with the same color as in the phase diagram of Figure 4. The solid red line shows ΔH , while the dashed blue line corresponds to the energy term ΔE . The orange dotted line is the pressure term $P\Delta V$. The green short-dashed line corresponds to the entropy contribution $-T\Delta S$ at 700 K.

introduces a nearly constant shift in ΔG , and thereby is ultimately responsible for reducing the formation Gibbs free energy of CuBi to negative values at elevated temperature and pressures above 7 GPa.

An analogous analysis of $\text{Cu}_{11}\text{Bi}_7$ shown in the lower panel of Figure 5 indicates a completely different stabilization mechanism. In contrast to CuBi, the $P\Delta V$ term is always negative at finite pressures due to the smaller atomic volume of $\text{Cu}_{11}\text{Bi}_7$ as compared to Cu + Bi. Therefore, it is only a matter of increasing the pressure sufficiently until the $P\Delta V$ term dominates the formation enthalpy, leading to the thermodynamic stability of $\text{Cu}_{11}\text{Bi}_7$ without any need to include entropic effects. However, the negative values of the entropic contribution $-T\Delta S$ support in lowering the transition pressure significantly with increasing temperatures.

Calculated Superconducting Properties. We further investigated the superconducting properties at 0 GPa based on the Allán–Dynes modified McMillan’s approximation of the Eliashberg equation.⁴² We recently reported similar calculations for $\text{Cu}_{11}\text{Bi}_7$ using a Coulomb pseudopotential value of $\mu^* = 0.13$, which gave a T_c in excellent agreement with the experimental value of $T_c = 1.36$ K. Using the same μ^* for CuBi, we obtain a superconducting transition temperature of $T_c = 1.7$ K. This is slightly higher than the experimental value of $T_c = 1.3$ K (Figure S9), which was also reported in ref 21. This discrepancy in T_c of around 0.4 K lies well within the expected accuracy of DFT calculations, and can be readily corrected by using a slightly higher value of μ^* . Using $\mu^* = 0.14$ lowers the T_c to 1.5 K, whereas $\mu^* = 0.15$ yields $T_c = 1.4$ K. The electron–phonon coupling constant of $\lambda = 0.67$ is comparable to the value of $\lambda = 0.63$ computed for $\text{Cu}_{11}\text{Bi}_7$. One potential reason for this slight overestimation of the T_c is that semilocal DFT

fails to correctly describe van der Waals interactions, which contribute strongly to holding together the CuBi layers as recently demonstrated by Amsler et al.⁴¹ A theoretically predicted isolated single sheet of CuBi, called cubine, has a lower value of $T_c < 1$ K and can be interpreted as a lower bound for the real transition temperature.

The upper panel of Figure 6 shows both the Eliashberg spectral function, $\alpha^2F(\omega)$, and the frequency-dependent

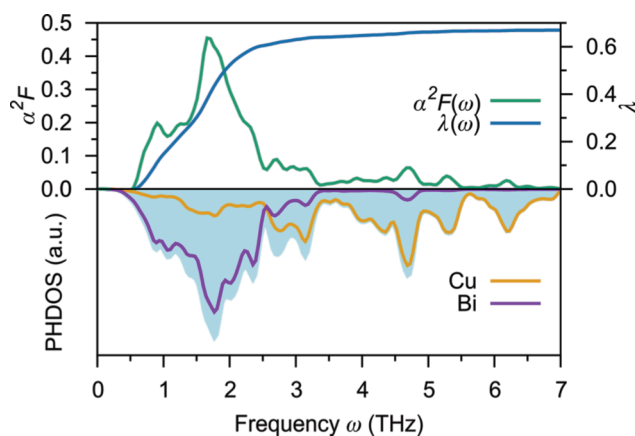


Figure 6. Electron–phonon coupling properties of CuBi at 0 GPa. The Eliashberg spectral function and the integrated coupling constant are shown in the top panel, whereas the partial PHDOS is shown in the lower panel. The shaded area indicates the total PHDOS.

coupling constant $\lambda(\omega)$. It is evident that phonons in the frequency range between 0 and 3 THz contribute primarily to the overall coupling strength. This low energy range is in fact strongly dominated by the Bi vibrations, as indicated in the lower panel of Figure 6, where the total phonon density of states (PHDOS) together with the partial, atom projected PHDOS are shown. Again, this behavior is consistent with the calculations in $\text{Cu}_{11}\text{Bi}_7$, where the Bi atoms mainly contribute to the electron–phonon coupling. We tentatively attribute the similarity in critical temperatures to the similar Bi framework found in the two compounds.

CONCLUSIONS

The foregoing results describe the efficacy of synthesis experiments performed in a DAC, which allow for in situ powder X-ray diffraction at high-*PT* conditions. These experiments provide valuable insight into the formation dynamics of CuBi and $\text{Cu}_{11}\text{Bi}_7$ and pave the way toward efficient intermetallic materials discovery in high-pressure phase space. Computational studies demonstrate that the stereochemically active lone pairs on the Bi atoms influence the structure of both unusual binary compounds. These lone pairs create channels and layers in $\text{Cu}_{11}\text{Bi}_7$ and CuBi, respectively. To further investigate these structure details, we analyzed the electronic structure and chemical bonding of these compounds by analyzing the ELF, which confirm our assignment of stereochemically active lone pairs on the Bi atoms. DFT calculations independently confirm experimental results, indicating that CuBi is the lower-pressure-stabilized phase. Further, we predict superconductivity in CuBi, with a transition temperature comparable to the experimentally observed value. Future work will focus on stabilizing these phases using ambient-pressure synthetic techniques.

EXPERIMENTAL SECTION

Synthesis of Bulk Samples. Sample synthesis and characterization of $\text{Cu}_{11}\text{Bi}_7$ is described elsewhere.²⁰ The bulk synthesis of CuBi is described below. Note, the in situ experiments, which also resulted in the formation of CuBi and $\text{Cu}_{11}\text{Bi}_7$, are described in a subsequent section. Metal reagents were purchased from commercial vendors and used as received. Sample synthesis proceeded by mechanical ball milling the elements to create a uniform powder, followed by high-pressure synthesis in a multianvil press. In a dinitrogen atmosphere, a 50 mL agate ball-milling crucible was charged with Cu powder (5.5 mmol, 0.3496 g), Bi powder (5.5 mmol, 1.1505 g), and seven alumina balls. Ball milling was performed for 4 h at a rate of 250 rpm using a Retsch planetary ball mill PM 100. Milling was stopped for 30 min every hour to allow for the dissipation of heat and to prevent cold welding. High-pressure reactions were performed using the 1000-ton multi-anvil press (MAP) at 13-ID-D, GeoSoilEnviroCARS (Sector 13), Advanced Photon Source (APS), Argonne National Laboratory. The 14/8 “G2” COMPRES cell assembly used for these reactions is described in detail elsewhere.⁴³ We modified this reaction setup by using a boron nitride crucible as a reaction container, which is more inert to reaction with metals than the standard magnesium oxide crucible (Figure S1). The highest purity samples were obtained via the following procedure. Samples were compressed to 135 tons over 4 h, which corresponds to a sample pressure of 4 GPa based on previously obtained calibration curves. The pressure was held for 15 min at ambient temperature. Samples were then heated using a resistive heater at a power output of 150 W. The thermocouple reported a temperature of 250 °C. Samples were annealed for 5 min and then rapidly cooled to room temperature by turning off the heater’s power supply. The pressure was released steadily over 5 h. The resulting samples were cylindrical in shape, with a diameter of ~1.5 mm and a height of ~1.5 mm with a silver–metallic color.

Crystallographic and Elemental Characterization. Scanning electron microscopy (SEM) was performed on a Hitachi S-3400N-II using a 25 kV electron beam and energy-dispersive X-ray spectroscopy (EDS) for semiquantitative elemental analysis was acquired with an Oxford INCAx-act SSD. Samples were mounted on conductive carbon tape on aluminum stages. Seventeen points over a $\sim 150 \mu\text{m} \times 100 \mu\text{m}$ area were averaged to obtain a composition of $\text{Cu}_{48.9(7)}\text{Bi}_{51.1(7)}$, which corresponds to an atomic formula of $\text{Cu}_{0.98(1)}\text{Bi}_{1.02(1)}$ when scaled to the formula unit. The samples are well sintered as shown by the secondary electron images, which feature a very small amount of cracks and crevices (Figure S6). Small Cu- and Bi-rich areas are seen in the SEM images.

The structure of CuBi was solved by Rietveld refinement of the synchrotron powder X-ray diffraction (PXRD) pattern from the high-resolution 11-BM diffractometer at the Advanced Photon Source, Argonne National Laboratory, with an incident wavelength of $\lambda = 0.414203 \text{ \AA}$. The samples were coated on the outside of a Kapton capillary using Dow Corning #4 electrical insulating grease, cooled to 100 K, and spun at $\sim 600 \text{ rpm}$ during collection. Powder diffraction data were analyzed by the Rietveld method using the computer program TOPAS.⁴⁴ The pattern was fit in the 2θ range of 2–40, and the background was fit using a Chebyshev polynomial with 30 parameters. Unreacted elemental Bi and Cu were fit along with the new phase. Stephens model line broadening was employed for each phase. The peaks corresponding to the new phase can be indexed to the orthorhombic space group $Pnma$ with unit cell parameters $a = 5.18898(2) \text{ \AA}$, $b = 4.23079(1) \text{ \AA}$, and $c = 7.86656(2) \text{ \AA}$. A search of the Inorganic Crystal Structure Database (ICSD)²⁵ listed $\text{Mn}(\text{Bi}_{0.85}\text{Sb}_{0.15})$ as having similar symmetry and lattice parameters ($Pnma$, $a = 5.70 \text{ \AA}$, $b = 4.27 \text{ \AA}$, and $c = 7.40 \text{ \AA}$).^{26,27} We used the atomic positions from this structure as a starting point for the refinement of CuBi . Further details are found in the Supporting Information. The synchrotron PXRD pattern indicates near complete conversion of the elements into CuBi (88.80%) with a small amount of residual elemental Cu (8.31%) and Bi (2.88%) (Figure S4).

Details of In Situ Experiments. All of the in situ laser heating and synchrotron powder X-ray diffraction (PXRD) experiments were

performed at Beamline 16-ID-B, HPCAT, Advanced Photon Source (APS), Argonne National Laboratory, IL. During the reaction experiments, samples were heated using an in situ double-sided laser heating setup.⁴⁵ High intensity monochromatic synchrotron radiation with a fixed wavelength of 0.406626 \AA was used for all diffraction experiments. Details of diamond anvil cell design can be found in the Supporting Information.

Computational Methods. Density functional theory (DFT) calculations were carried out within the projector augmented wave (PAW) formalism⁴⁶ as implemented in the VASP package^{47–49} together with the Perdew–Burke–Ernzerhof (PBE) approximation to the exchange correlation potential.⁵⁰ A plane-wave cutoff energy of 400 eV was used with a sufficiently dense k -point mesh to ensure a convergence of the total energy to within 4 meV/atom. Both the atomic and the cell parameters were simultaneously relaxed until the maximal force components were less than 4 meV/Å. The free energy contributions were evaluated from the vibrational entropy computed at every pressure in steps of 1 GPa.

Structural searches were carried out with the Minima Hopping method (MHM)^{51,52} using the Minihocao package, which implements a highly reliable algorithm to identify the low-energy (at $P = 0$) or low-enthalpy (at high P) structure of compounds solely given the chemical composition.^{53–56} The energy/enthalpy landscape is explored by performing consecutive molecular dynamics trial steps followed by local geometry relaxations. The Bell–Evans–Polanyi principle is exploited by aligning the initial molecular dynamics velocities along soft mode directions to accelerate the search.^{57,58} MHM simulations were carried out at fixed pressures of 0 and 10 GPa, and the most promising candidate structures were subsequently relaxed at variable pressures to assess the complete enthalpy diagram.

Phonon calculations were carried out with the frozen phonon approach as implemented in the PHONOPY package using sufficiently large supercells for converged thermal properties.⁵⁹ To compute the vibrational contribution to the free energy, a dense k -point mesh of $30 \times 30 \times 30$ was used to sample the Brillouin zone. The harmonic free energy at temperature T was computed according to

$$F(T) = E + \int \frac{\hbar\omega}{2} g(\omega) d\omega + \int k_B T \ln(1 - e^{-(\hbar\omega/k_B T)}) g(\omega) d\omega$$

where E is the internal energy, and $g(\omega)$ is the phonon density of states at frequency ω .

The Quantum Espresso package was used to compute the phonon-mediated superconducting properties.⁶⁰ We used ultrasoft pseudopotentials and a plane-wave cutoff energy of 40 Ry. The Allan–Dynes modified McMillan’s approximation of the Eliashberg equation⁶¹ was used to estimate the superconducting temperature:

$$T_c = \frac{\omega_{\log}}{1.2} \exp\left[-\frac{1.04(1 + \lambda)}{\lambda - \mu^*(1 + 0.62\lambda)}\right]$$

where μ^* is the Coulomb pseudopotential, λ is the overall electron–phonon coupling strength computed from the frequency dependent Eliashberg spectral function $\alpha^2 F(\omega)$, and ω_{\log} is the logarithmic average phonon frequency. A $6 \times 6 \times 4$ q -mesh was used together with a denser $24 \times 24 \times 16$ k -mesh for the $Pnma$ structure, resulting in a well-converged superconducting transition temperature T_c . A value of $\mu^* = 0.13$ was employed, which was shown to give a T_c in excellent agreement with experimental results obtained for $\text{Cu}_{11}\text{Bi}_7$.²⁰ The phonon density of states in Figure 6 was computed using PHONOPY based on force constants obtained through the linear response calculations with Quantum Espresso.

ASSOCIATED CONTENT

Supporting Information

The Supporting Information is available free of charge on the ACS Publications website at DOI: 10.1021/acs.chemmater.7b01418.

Experimental details, differential scanning calorimetry, scanning electron microscopy, temperature–pressure

formation free energies, and Rietveld refinement parameters (PDF)
X-ray crystallographic data for CuBi (CIF)

AUTHOR INFORMATION

Corresponding Authors

*E-mail: c-wolverton@northwestern.edu.

*E-mail: danna.freedman@northwestern.edu.

ORCID

Steven D. Jacobsen: 0000-0002-9746-958X

Chris Wolverton: 0000-0003-2248-474X

Danna E. Freedman: 0000-0002-2579-8835

Author Contributions

#S.M.C. and M.A. contributed equally.

Notes

The authors declare no competing financial interest.

ACKNOWLEDGMENTS

The collaborative project between D.E.F., C.W., and S.D.J. is supported by Northwestern through the Innovative Initiatives Incubator (I3). This experimental work is supported by the AFOSR (FA95501410358), and used resources of the APS (DOE: DE-AC02-06CH11357). GeoSoilEnviroCARS at the APS is supported by the NSF (EAR-1128799) and DOE (DE-FG02-94ER14466). S.M.C. acknowledges support from the NSF GRFP (DGE-1324585). M.A. and C.W. (DFT calculations) acknowledge support from the Novartis Universität Basel Excellence Scholarship for Life Sciences and the Swiss National Science Foundation (P300P2-158407) and DOE (DE-FG02-07ER46433). Computational resources from the Swiss National Supercomputing Center in Lugano (Project s700), the Extreme Science and Engineering Discovery Environment (XSEDE) (which is supported by National Science Foundation grant number OCI-1053575), the Bridges system at the Pittsburgh Supercomputing Center (PSC) (which is supported by NSF award number ACI-1445606), the Quest high performance computing facility at Northwestern University, and the National Energy Research Scientific Computing Center (DOE: DE-AC02-05CH11231) are gratefully acknowledged. S.D.J. acknowledges support from NSF (DMR-1508577) and the Carnegie/DOE Alliance Center (CDAC) for providing beamtime at HPCAT. HPCAT operations are supported by DOE-NNSA under award no. DE-NA0001974, with partial instrumentation funding by NSF. Y.M. acknowledges the support of DOE-BES/DMSE under award no. DE-FG02-99ER45775. This work made use of the IMSERC at Northwestern University, which has received support from the Soft and Hybrid Nanotechnology Experimental (SHyNE) Resource (NSF NNCI-1542205), the State of Illinois and International Institute for Nanotechnology (IIN).

REFERENCES

- (1) Tafti, F. F.; Torikachvili, M. S.; Stillwell, R. L.; Baer, B.; Stavrou, E.; Weir, S. T.; Vohra, Y. K.; Yang, H.-Y.; McDonnell, E. F.; Kushwaha, S. K.; Gibson, Q. D.; Cava, R. J.; Jeffries, J. R. Tuning the Electronic and the Crystalline Structure of LaBi by Pressure. *Phys. Rev. B: Condens. Matter Phys.* **2017**, *95*, 014507.
- (2) Walsh, J. P. S.; Clarke, S. M.; Meng, Y.; Jacobsen, S. D.; Freedman, D. E. Discovery of FeBi₂. *ACS Cent. Sci.* **2016**, *1*, 668–669.
- (3) Amsler, M.; Naghavi, S. S.; Wolverton, C. Prediction of Superconducting Iron–Bismuth Intermetallic Compounds At High Pressure. *Chem. Sci.* **2017**, *8*, 2226–2234.

(4) Oganov, A. R. *Modern Methods of Crystal Structure Prediction*; Wiley-VCH: New York, 2011.

(5) Yang, F. Y.; Liu, K.; Hong, K.; Reich, D. H.; Searson, P. C.; Chien, C. L. Large Magnetoresistance of Electrodeposited Single-Crystal Bismuth Thin Films. *Science* **1999**, *284*, 1335–1337.

(6) Tian, M.; Wang, J.; Kumar, N.; Han, T.; Kobayashi, Y.; Liu, Y.; Mallouk, T. E.; Chan, M. H. W. Observation of Superconductivity in Granular Bi Nanowires Fabricated by Electrodeposition. *Nano Lett.* **2006**, *6*, 2773–2780.

(7) Li, L.; Checkelsky, J. G.; Hor, Y. S.; Uher, C.; Hebard, A. F.; Cava, R. J.; Ong, N. P. Phase Transitions of Dirac Electrons in Bismuth. *Science* **2008**, *321*, 547–550.

(8) Prakash, O.; Kumar, A.; Thamizhavel, A.; Ramakrishnan, S. Evidence for Bulk Superconductivity in Pure Bismuth Single Crystals at Ambient Pressure. *Science* **2017**, *355*, 52–55.

(9) Matthias, B. T.; Jayaraman, A.; Geballe, T. H.; Andres, K.; Corenzwit, E. Many More Superconducting Bismuth Phases. *Phys. Rev. Lett.* **1966**, *17*, 640–643.

(10) Kanatzidis, M. G.; Pöttgen, R.; Jeitschko, W. The Metal Flux: A Preparative Tool for the Exploration of Intermetallic Compounds. *Angew. Chem., Int. Ed.* **2005**, *44*, 6996–7023.

(11) Thompson, C. M.; Tan, X.; Kovnir, K.; Garlea, V. O.; Gippius, A. A.; Yaroslavtsev, A. A.; Menushenkov, A. P.; Chernikov, R. V.; Buttgen, N.; Kratschmer, W.; Zubavichus, Y. V.; Shatruk, M. Synthesis, Structures, and Magnetic Properties of Rare-Earth Cobalt Arsenides, RCo₂As₂ (R = La, Ce, Pr, Nd). *Chem. Mater.* **2014**, *26*, 3825–3837.

(12) Phelan, W. A.; Nguyen, G. V.; Wang, J. K.; McCandless, G. T.; Morosan, E.; DiTusa, J. F.; Chan, J. Y. Discovery of Spin Glass Behavior in Ln₂Fe₄Sb₅ (Ln = La–Nd and Sm). *Inorg. Chem.* **2012**, *51*, 11412–11421.

(13) Thompson, C. M.; Kovnir, K.; Eveland, S.; Herring, M. J.; Shatruk, M. Synthesis of ThCrSi₂-Type Arsenides from Bi Flux. *Chem. Commun.* **2011**, *47*, 5563–5563.

(14) Brugger, R. M.; Bennion, R. B.; Worlton, T. G. The Crystal Structure of Bismuth-II at 26 Kbar. *Phys. Lett. A* **1967**, *24*, 714–717.

(15) Chen, J. H.; Iwasaki, H.; Kikegawa, T.; Yaoita, K.; Tsuji, K. Crystal Structure of the High Pressure Phase of Bismuth BiIII. *AIP Conf. Proc.* **1993**, *309*, 421–424.

(16) Degtyareva, O.; McMahan, M. I.; Nelmis, R. J. Crystal Structure of the High Pressure Phase of Bismuth Bi-III. *Mater. Sci. Forum* **2001**, *378–381*, 469–475.

(17) Chaimayo, W.; Lundegaard, L. F.; Loa, I.; Stinton, G. W.; Lennie, A. R.; McMahan, M. I. High-Pressure, High-Temperature Single-Crystal Study of Bi-IV. *High Pressure Res.* **2012**, *32*, 442–449.

(18) Schaufelberger, P.; Merx, H.; Contre, M. Structure Cristalline Du Bismuth V. *High Temp. Pressure* **1973**, *5*, 221–230.

(19) Klement, W.; Jayaraman, A.; Kennedy, G. C. Phase Diagram of Arsenic, Antimony, and Bismuth at Pressures up to 70 Kbars. *Phys. Rev.* **1963**, *131*, 632–637.

(20) Clarke, S. M.; Walsh, J. P. S.; Amsler, M.; Malliakas, C. D.; Yu, T.; Goedecker, S.; Wang, Y.; Wolverton, C.; Freedman, D. E. Discovery of a superconducting Cu–Bi compound by high-pressure synthesis. *Angew. Chem., Int. Ed.* **2016**, *55*, 13446–13449.

(21) Guo, K.; Akselrud, L.; Bonbar, M.; Burkhardt, U.; Schmidt, M.; Zhao, J.-T.; Schwarz, U.; Grin, Y. Weak Interactions Under Pressure: hp-CuBi and Its Analogues. *Angew. Chem., Int. Ed.* **2017**, *56*, 5620.

(22) Speziale, S.; Zha, C.-S.; Duffy, T. S.; Hemley, R. J.; Mao, H.-K. Quasi-hydrostatic compression of magnesium oxide to 52 GPa: Implications for the pressure–volume–temperature equation of state. *J. Geophys. Res.: Solid Earth* **2001**, *106*, 515–528.

(23) Meng, Y.; Hrubiak, R.; Rod, E.; Boehler, R.; Shen, G. New Developments in Laser-Heated Diamond Anvil Cell with in Situ Synchrotron X-Ray Diffraction at High Pressure Collaborative Access Team. *Rev. Sci. Instrum.* **2015**, *86*, 72201.

(24) Akella, J.; Kennedy, G. C. Melting of Gold, Silver, and Copper—proposal for a New High-Pressure Calibration Scale. *J. Geophys. Res.* **1971**, *76*, 4969–4977.

(25) Inorganic Crystal Structure Database (ICSD) Web, Version 3.5.0; FIZ Karlsruhe: Germany, 2017.

- (26) Göbel, H.; Wolfgang, E.; Harms, H. Properties of MnBi Compounds Partially Substituted with Cu, Zn, Ti, Sb, and Te. I. Formation of Mixed Phases and Crystal Structures. *Phys. Status Solidi* **1976**, *34*, 553–564.
- (27) Cenxual, K.; Gelato, L. M.; Penzo, M.; Parthe, E.; Parthé, E. Inorganic Structure Types with Revised Space Groups. I. *Acta Crystallogr., Sect. B: Struct. Sci.* **1991**, *47*, 433–439.
- (28) Alsen, N. Röntgenographische Untersuchungen der Kristallstrukturen von Magnetkies, Breithauptit, Pentlandit, Millerit und verwandten Verbindungen. *Geol. Foeren. Stockholm Foerh.* **1925**, *47*, 19–73.
- (29) James, A. M.; Lord, M. P. *Macmillan's Chemical and Physical Data*; Macmillan Press: London, 1992.
- (30) CN was computed from Cu–Cu distances below 2.66 Å and Cu–Bi distances below 2.88 Å.
- (31) Kalychak, Y. M.; Zaremba, V. I.; Pecharsky, V. K. Crystal Structure of Terbium Cobalt Indium (1/2/1), TbCo₂In. *Z. Kristallogr. - Cryst. Mater.* **1993**, *205*, 333–334.
- (32) Willis, B. T. M.; Rooksby, H. P. Magnetic Transitions and Structural Changes in Hexagonal Manganese Compounds. *Proc. Phys. Soc., London, Sect. B* **1954**, *67*, 290–296.
- (33) Lidin, S.; Petricek, V.; Stenberg, L.; Furuseth, S.; Fjellvag, H.; Larsson, A.-K. The Incommensurately Modulated Structure of NiBi. *Solid State Sci.* **2000**, *2*, 353–363.
- (34) Ruck, M. Die Kristallstruktur von BiNi: Eine Komplexe Ausdünnungsvariante Des InNi₂-Typs. *Z. Anorg. Allg. Chem.* **1999**, *625*, 2050–2054.
- (35) Walsh, A.; Payne, D. J.; Egdell, R. G.; Watson, G. W. Stereochemistry of Post-Transition Metal Oxides: Revision of the Classical Lone Pair Model. *Chem. Soc. Rev.* **2011**, *40*, 4455–4463.
- (36) Grin, Y.; Wedig, U.; von Schnering, H. G. Hyperbolic Lone Pair Structure in RhBi₄. *Angew. Chem., Int. Ed. Engl.* **1995**, *34*, 1204–1206.
- (37) Isaeva, A.; Ruck, M.; Schäfer, K.; Rodewald, U. C.; Pöttgen, R. Structure and Bonding of Bi₄Ir: A Difficult-to-Access Bismuth Iridide with a Unique Framework Structure. *Inorg. Chem.* **2015**, *54*, 885–889.
- (38) Zhang, W.; Oganov, A. R.; Goncharov, A. F.; Zhu, Q.; Bouffelfel, S. E.; Lyakhov, A. O.; Stavrou, E.; Somayazulu, M.; Prakapenka, V. B.; Konpkov, Z. Unexpected Stable Stoichiometries of Sodium Chlorides. *Science* **2013**, *342*, 1502.
- (39) Dong, X.; Oganov, A. R.; Goncharov, A. F.; Stavrou, E.; Lobanov, S.; Saleh, G.; Qian, G. R.; Zhu, Q.; Gatti, C.; Deringer, V. L.; Dronskowski, R.; Zhou, X. F.; Prakapenka, V. B.; Konôpková, Z.; Popov, I. A.; Boldyrev, A. I.; Wang, H. T. A Stable Compound of Helium and Sodium at High Pressure. *Nat. Chem.* **2017**, *9*, 440.
- (40) Häussermann, U.; Söderberg, K.; Norrestam, R. Comparative Study of the High-Pressure Behavior of As, Sb, and Bi. *J. Am. Chem. Soc.* **2002**, *124*, 15359–15367.
- (41) Amsler, M.; Yao, Z.; Wolverson, C. *Cubine, A Superconducting 2-Dimensional Copper-Bismuth Nano Sheet*, 2017; arXiv:1703.03038.
- (42) Allen, P. B.; Dynes, R. C. Transition Temperature of Strong-Coupled Superconductors Reanalyzed. *Phys. Rev. B* **1975**, *12*, 905–922.
- (43) Leinenweber, K. D.; Tyburczy, J. A.; Sharp, T. G.; Soignard, E.; Diedrich, T.; Petuskey, W. B.; Wang, Y.; Mosenfelder, J. L. Cell assemblies for reproducible multi-anvil experiments (the COMPRES assemblies). *Am. Mineral.* **2012**, *97*, 353.
- (44) Coelho, A. A. *TOPAS Academic: General Profile and Structure Analysis Software for Powder Diffraction Data*; Bruker AXS: Karlsruhe, Germany, 2007.
- (45) Meng, Y.; Hrubciak, R.; Rod, E.; Boehler, R.; Shen, G. New Developments in Laser-Heated Diamond Anvil Cell with *In Situ* Synchrotron X-ray Diffraction at High Pressure Collaborative Access Team. *Rev. Sci. Instrum.* **2015**, *86*, 072201.
- (46) Blöchl, P. E. Projector Augmented-Wave Method. *Phys. Rev. B: Condens. Matter Mater. Phys.* **1994**, *50*, 17953.
- (47) Kresse, G. Ab Initio Molecular Dynamics for Liquid Metals. *J. Non-Cryst. Solids* **1995**, *192*, 222.
- (48) Kresse, G.; Furthmüller, J. Efficiency of Ab-Initio Total Energy Calculations for Metals and Semiconductors Using a Plane-Wave Basis Set. *Comput. Mater. Sci.* **1996**, *6*, 15.
- (49) Kresse, G.; Joubert, D. From Ultrasoft Pseudopotentials to the Projector Augmented-Wave Method. *Phys. Rev. B: Condens. Matter Mater. Phys.* **1999**, *59*, 1758.
- (50) Perdew, J. P.; Burke, K.; Ernzerhof, M. Generalized Gradient Approximation Made Simple. *Phys. Rev. Lett.* **1996**, *77*, 3865.
- (51) Amsler, M.; Goedecker, S. Crystal Structure Prediction Using the Minima Hopping Method. *J. Chem. Phys.* **2010**, *133*, 224104.
- (52) Goedecker, S. Minima Hopping: An Efficient Search Method for the Global Minimum of the Potential Energy Surface of Complex Molecular Systems. *J. Chem. Phys.* **2004**, *120*, 9911.
- (53) Amsler, M.; Flores-Livas, J. A.; Lehtovaara, L.; Balima, F.; Ghasemi, S. A.; Machon, D.; Pailhès, S.; Willand, A.; Caliste, D.; Botti, S.; San Miguel, A.; Goedecker, S.; Marques, M. A. L. Crystal Structure of Cold Compressed Graphite. *Phys. Rev. Lett.* **2012**, *108*, 065501.
- (54) Amsler, M.; Botti, S.; Marques, M. A. L.; Lenosky, T. J.; Goedecker, S. Low-Density Silicon Allotropes for Photovoltaic Applications. *Phys. Rev. B: Condens. Matter Mater. Phys.* **2015**, *92*, 014101.
- (55) Amsler, M.; Flores-Livas, J. A.; Huan, T. D.; Botti, S.; Marques, M. A. L.; Goedecker, S. Novel Structural Motifs in Low Energy Phases of LiAlH₄. *Phys. Rev. Lett.* **2012**, *108*, 205505.
- (56) Flores-Livas, J. A.; Amsler, M.; Heil, C.; Sanna, A.; Boeri, L.; Profeta, G.; Wolverson, C.; Goedecker, S.; Gross, E. K. U. Superconductivity in Metastable Phases of Phosphorus-Hydride Compounds under High Pressure. *Phys. Rev. B: Condens. Matter Mater. Phys.* **2016**, *93*, 020508.
- (57) Roy, S.; Goedecker, S.; Hellmann, V. Bell-Evans-Polanyi Principle for Molecular Dynamics Trajectories and Its Implications for Global Optimization. *Phys. Rev. E* **2008**, *77*, 056707.
- (58) Sicher, M.; Mohr, S.; Goedecker, S. Efficient Moves for Global Geometry Optimization Methods and Their Application to Binary Systems. *J. Chem. Phys.* **2011**, *134*, 044106–044106.
- (59) Togo, A.; Oba, F.; Tanaka, I. First-Principles Calculations of the Ferroelastic Transition between Rutile-Type and CaCl₂-Type SiO₂ at High Pressures. *Phys. Rev. B: Condens. Matter Mater. Phys.* **2008**, *78*, 134106.
- (60) Giannozzi, P.; Baroni, S.; Bonini, N.; Calandra, M.; Car, R.; Cavazzoni, C.; Ceresoli, D.; Chiarotti, G. L.; Cococcioni, M.; Dabo, I.; Corso, A. D.; de Gironcoli, S.; Fabris, S.; Fratesi, G.; Gebauer, R.; Gerstmann, U.; Gougoussis, C.; Kokalj, A.; Lazzeri, M.; Martin-Samos, L.; Marzari, N.; Mauri, F.; Mazzarello, R.; Paolini, S.; Pasquarello, A.; Paulatto, L.; Sbraccia, C.; Scandolo, S.; Sclauzero, G.; Seitsonen, A. P.; Smogunov, A.; Umari, P.; Wentzcovitch, R. M. QUANTUM ESPRESSO: A Modular and Open-Source Software Project for Quantum Simulations of Materials. *J. Phys.: Condens. Matter* **2009**, *21*, 395502.
- (61) Allen, P. B.; Dynes, R. C. Transition Temperature of Strong-Coupled Superconductors Reanalyzed. *Phys. Rev. B* **1975**, *12*, 905.